



## Efficient and stable CO<sub>2</sub> to formate conversion enabled by edge-site-enriched SnS<sub>2</sub> nanoplates

Zhipeng Liu <sup>a</sup>, Chang Liu <sup>a,b</sup>, Jiawei Zhang <sup>c</sup>, Suhua Mao <sup>a</sup>, Xiao Liang <sup>a</sup>, Hanlin Hu <sup>a</sup>, Xiaoxi Huang <sup>a,\*</sup>

<sup>a</sup> Hoffmann Institute of Advanced Materials, Postdoctoral Innovation Practice Base, Shenzhen Polytechnic, 7098 Liuxian Blvd, Nanshan District, Shenzhen 518055, PR China

<sup>b</sup> School of Chemical Engineering, University of Science and Technology Liaoning, Anshan 114051, PR China

<sup>c</sup> School of Rare Earths, University of Science and Technology of China, Hefei 230026, PR China



### ARTICLE INFO

#### Keywords:

CO<sub>2</sub> reduction reaction

Tin disulfide

Two-dimensional nanoflakes

Anisotropic activity

### ABSTRACT

Layered materials have been investigated in many different catalytic reactions due to their excellent functionalities. In particular, understanding the anisotropic properties of layered materials is important for the design of more efficient catalysts. Herein, SnS<sub>2</sub> nanoflakes with abundant edge sites (E-SnS<sub>2</sub>) were synthesized and their catalytic properties towards the electrochemical CO<sub>2</sub> reduction reaction (CO<sub>2</sub>RR) were studied. Combining experimental data and computational analysis, we found that the edge sites of SnS<sub>2</sub> are more active for CO<sub>2</sub> to formate conversion compared with the basal sites. Moreover, a CO<sub>2</sub> reduction intermediates triggered activation mechanism at the edge sites is proposed, the formation of sulfur vacancies at the edges would generate more active sites for CO<sub>2</sub>RR. The as-synthesized E-SnS<sub>2</sub> shows high selectivity, activity and robust stability for at least 12 h in a flow cell under a current density of  $-200 \text{ mA}\cdot\text{cm}^{-2}$ . This work may provide a new perspective on rational catalyst design for CO<sub>2</sub>RR.

### 1. Introduction

While fossil fuels boost the prosperity of modern industry, their consumption results in massive emission of carbon dioxides (CO<sub>2</sub>) and severe global environmental issues [1,2]. The electrochemical CO<sub>2</sub> reduction reaction (CO<sub>2</sub>RR) provides an appealing approach to mitigating the excessive CO<sub>2</sub> under ambient condition [3,4]. It enables the use of increasingly abundant renewable energy sources, such as solar and wind, to drive the conversion of CO<sub>2</sub> to renewable chemicals, thereby establishing a sustainable “carbon cycle” [5]. However, the overall energy conversion efficiency of CO<sub>2</sub>RR is limited by high activation energy barrier of CO<sub>2</sub> molecule, and the complicated reaction pathways lead to many different products [6–8]. Therefore, designing and developing CO<sub>2</sub> conversion electrocatalysts with high activity and selectivity is crucial for a feasible carbon cycling.

Among many different heterogeneous catalysts, layered materials have gained a lot of attention since the discovery of single-layer graphene in 2004 [9]. For example, transition metal dichalcogenides (TMDs) are typical layered materials widely applied to catalyze diverse

electrochemical reactions [10–14]. The relatively weak out-of-plane van der Waals interactions make it possible to engineer such materials with atomic thickness via exfoliation process, which endows them with large specific surface areas and tunable structural and electronic properties [15–19]. One of the most intriguing characteristics is the anisotropy, as the two dimensional structures have both strong in-plane chemical bonds and many edge dangling bonds [20–22]. Understanding the structure-activity relationship of basal and edge sites is crucial in order to design more efficient electrocatalyst. Researchers have identified that the edge sites of MoS<sub>2</sub> is catalytically more active than basal sites [23, 24]. Therefore, structural engineering strategies, such as reducing the lateral dimension to nanoscale [25], creating porous structures or tailoring the film orientations [26–28], are primarily conducted to expose more edge sites to promote catalytic activity.

Similar with 1 T-MoS<sub>2</sub>, tin disulfide (SnS<sub>2</sub>) is a layered material, wherein the metal atoms are sandwiched between alternate layers of sulfur atoms [29]. This material has been considered as a potential candidate for electrochemical CO<sub>2</sub> to formate conversion due to the tunable electronic structures and high surface to volume ratio [30–34].

\* Corresponding author.

E-mail address: [xiaoxihuang@szpt.edu.cn](mailto:xiaoxihuang@szpt.edu.cn) (X. Huang).

The basal plane of  $\text{SnS}_2$  exposes coordination saturated sulfur atoms only, while coordination unsaturated tin and sulfur atoms are exposed at edges. Due to such anisotropic structures, the edge sites and basal sites are expected to show different catalytic performance in  $\text{CO}_2\text{RR}$ . However, the active sites in  $\text{SnS}_2$  are still vague, in particular, it is still unclear whether the  $\text{CO}_2$  to formate conversion activity comes from the edge sites or basal sites.

To this end, edge-site-enriched  $\text{SnS}_2$  (E- $\text{SnS}_2$ ) and basal-site-enriched  $\text{SnS}_2$  (B- $\text{SnS}_2$ ) are synthesized to elucidate the active site toward  $\text{CO}_2\text{RR}$  in this report. Based on the measurements of  $\text{CO}_2\text{RR}$  activity and selectivity, catalyst structural characterization and theoretical simulations, the edge sites of  $\text{SnS}_2$  with sulfur vacancy are identified as the active centers for  $\text{CO}_2$  to formate conversion. Besides the remarkable selectivity and activity, E- $\text{SnS}_2$  is stable under an industrial grade of current density for at least 12 h.

## 2. Materials and methods

### 2.1. Materials and reagents

Tin chloride pentahydrate ( $\text{SnCl}_4 \cdot 5 \text{ H}_2\text{O}$ , AR), tin chloride dihydrate ( $\text{SnCl}_2 \cdot 2 \text{ H}_2\text{O}$ , AR), acetic acid ( $\text{HOAc}$ ) were supplied by Shanghai Aladdin Biochemical Co., Ltd. Nafion 117 solution (5 wt%) was supplied by Sigma Aldrich. Chemours (formerly DuPont) Nafion 117 proton exchange membranes were used during electrolysis. Thioacetamide (TAA) and potassium bicarbonate ( $\text{KHCO}_3$ ,  $\geq 99.99\%$  metals basis) were purchased from Shanghai Macklin Biochemical Co., Ltd. Carbon paper was purchased from Ce Tech Co., Ltd. High purity  $\text{CO}_2$  (99.999%) was used in electrochemical test.

### 2.2. Synthesis of E- $\text{SnS}_2$ and B- $\text{SnS}_2$

Edge rich  $\text{SnS}_2$  nano-flakes (E- $\text{SnS}_2$ ) were synthesized via a hydrothermal process. Typically, 3 mL of  $\text{HOAc}$  and 17 mL of water were mixed, then 0.1 mmol  $\text{SnCl}_2 \cdot 2 \text{ H}_2\text{O}$  and 2 mmol of  $\text{SnCl}_4 \cdot 5 \text{ H}_2\text{O}$  were dissolved in this  $\text{HOAc}$  solution after stirring for 30 mins at 50 °C. Afterwards, 10 mL aqueous solution containing 4.5 mmol of TAA was added dropwise under stirring. The transparent solution was sealed in a 50 mL Teflon lined autoclave and heat at 160 °C for 12 h. The product was collected with centrifugation, rinsed with water and ethanol for several times and then dried in vacuum at 60 °C. The ratio of  $\text{SnCl}_2 \cdot 2 \text{ H}_2\text{O}$  was adjusted to generate various samples with different morphology. Basal plane rich nanosheets (B- $\text{SnS}_2$ ) were synthesized and utilized as a reference sample following the similar route, but the volume of  $\text{HOAc}$  was elevated to 10 mL and the amount of water was reduced to 10 mL.

The exfoliation of E- $\text{SnS}_2$  was conducted via a previously reported method [35]. Typically, 80 mg of E- $\text{SnS}_2$  was added into 50 mL formamide and then refluxed at 110 °C for 24 h. Differential centrifugation was conducted to separate  $\text{SnS}_2$  in different thickness at 500 rpm for 20 min, 5000 rpm for 5 min and 15000 for 8 min, respectively. The sample collected at 500 rpm and 15000 rpm were then dried in vacuum overnight for further characterization.

### 2.3. Characterization

Electron microscope images and elemental mappings were collected using a transmission electron microscope (TEM, JEOL JEM 2100 F) and a field emission scanning electron microscope (FESEM, JEOL JSM-IT800 (SHL)). High-angle annular dark-field imaging scanning transmission electron microscopy (HADDF-STEM) was obtained on a FEI Themis Z spherical aberration electron microscope at 200 kV acceleration voltage. Atomic force microscopy (AFM) was performed by means of Bruker Dimension Icon atomic force microscope. X-ray powder diffraction (XRD) patterns were recorded on a Bruker D8 Advanced X-ray diffractometer using Cu K $\alpha$  radiation source ( $\lambda = 0.15418 \text{ nm}$ ). X-ray

photoelectron spectroscopy (XPS) was conducted on a ThermoFisher Nexsa X-Ray photoelectron spectrometer with Al K $\alpha$  excitation source. In-situ FTIR spectra was measured on Nicolet 6700 with MCT detector. The concentrations of different elements in the samples were determined using an Inductively Coupled Plasma Optical Emission Spectrometer (ICP-OES, Agilent 720ES).

### 2.4. Electrochemical measurements

The electrochemical measurements were conducted in a typical three-electrode system. A Ag/AgCl electrode filled with 3 M KCl and a piece of platinum foil ( $1 \times 1 \text{ cm}^2$ ) were used as reference and counter electrode, respectively. An electrocatalyst ink was prepared by dispersing 10 mg of electrocatalyst in 1 mL ethanol and 80  $\mu\text{L}$  of Nafion solution (5 wt%) via ultrasonication. For working electrode tested in H type cell, 200  $\mu\text{L}$  of the uniform electrocatalyst ink was sprayed on porous carbon paper (GDL210S, Ce Tech Co., Ltd.), of which  $1 \times 1 \text{ cm}^2$  area is accessible to electrolyte. The cathodic and anodic chambers of H-cell were separated by a Nafion proton exchange membrane and filled with 60 mL of 0.5 M  $\text{KHCO}_3$  electrolyte. The electrolyte in cathodic chamber was bubbled by high-purity  $\text{CO}_2$  before and during electrochemical measurements at a constant rate (10 sccm). The cathodic electrolyte was stirred at 350 rpm. Cyclic voltammetry was recorded at 0 to  $-1.2 \text{ V}$  vs RHE to reveal the redox features of pristine electrocatalyst. To achieve a stable catalytic performance, electrocatalysts were reduced at  $-0.7 \text{ V}$  vs RHE for 0.5 h and potentiostatic electrolysis was subsequently conducted at different potentials ranging from  $-0.6$  to  $-1.2 \text{ V}$  vs RHE with a duration of 2 h at each potential. In regard to flow cell test, working electrode was prepared by spaying 500  $\mu\text{L}$  of the electrocatalyst ink on a ( $1.5 \times 2.5 \text{ cm}^2$ ) carbon paper. For stability evaluation, 10 mg of the electrocatalyst was loaded on a ( $1.5 \times 2.5 \text{ cm}^2$ ) carbon paper (GDL210SHT, Ce Tech Co., Ltd.). The carbon paper was sandwiched between cathodic and gas chamber with  $1 \text{ cm}^2$  geometric area exposed to cathodic electrolyte. A proton exchange membrane (Nafion 117) was used to separate anodic and cathodic chamber. 1 M KOH electrolyte was pumped into the cathodic and anodic chambers and the  $\text{CO}_2$  electroreduction was evaluated with constant  $\text{CO}_2$  gas feed rate of 30 sccm.

### 2.5. Products analysis

The products were analyzed according to our previous reports [36]. Hydrogen and carbon monoxide were quantified via online gas chromatography (Agilent 7890B) with an interval of 25 mins during bulk electrolysis for two hours. Formate concentration in the electrolyte was quantified by nuclear magnetic resonance chemical analyzer (JEOL JEM-ECZ400S/L1).

### 2.6. DFT calculation details

The spin polarized periodic DFT calculations were performed at the GGA-PBE level using the MedeA VASP (Vienna ab-initio simulation package) [37–40]. A  $\text{SnS}_2$  monolayer composed of 48 atoms ( $\text{Sn}_{16}\text{S}_{32}$ ) was constructed as model slab for the calculation. The slab exposes both basal plane and edges. The vacuum space perpendicular to the basal plane is  $\sim 15 \text{ \AA}$ . The structural optimizations were performed using a k-spacing of 0.3 per Angstrom (corresponding to a  $2 \times 1 \times 1$  mesh) and a plane-wave cut-off energy of 400 eV. The DFT+D3 approach of S. Grimme with zero-damping was used to describe Van der Waals interactions [41]. During the geometry optimization, all the atoms including adsorbates were allowed to relax until the residual force on each ion was lower than 0.01 eV/Ångstrom. The electronic iterations convergence is  $1 \times 10^{-5} \text{ eV}$ .

The following  $\text{CO}_2\text{RR}$  mechanism was considered for the theoretical calculations:

Formic Acid:

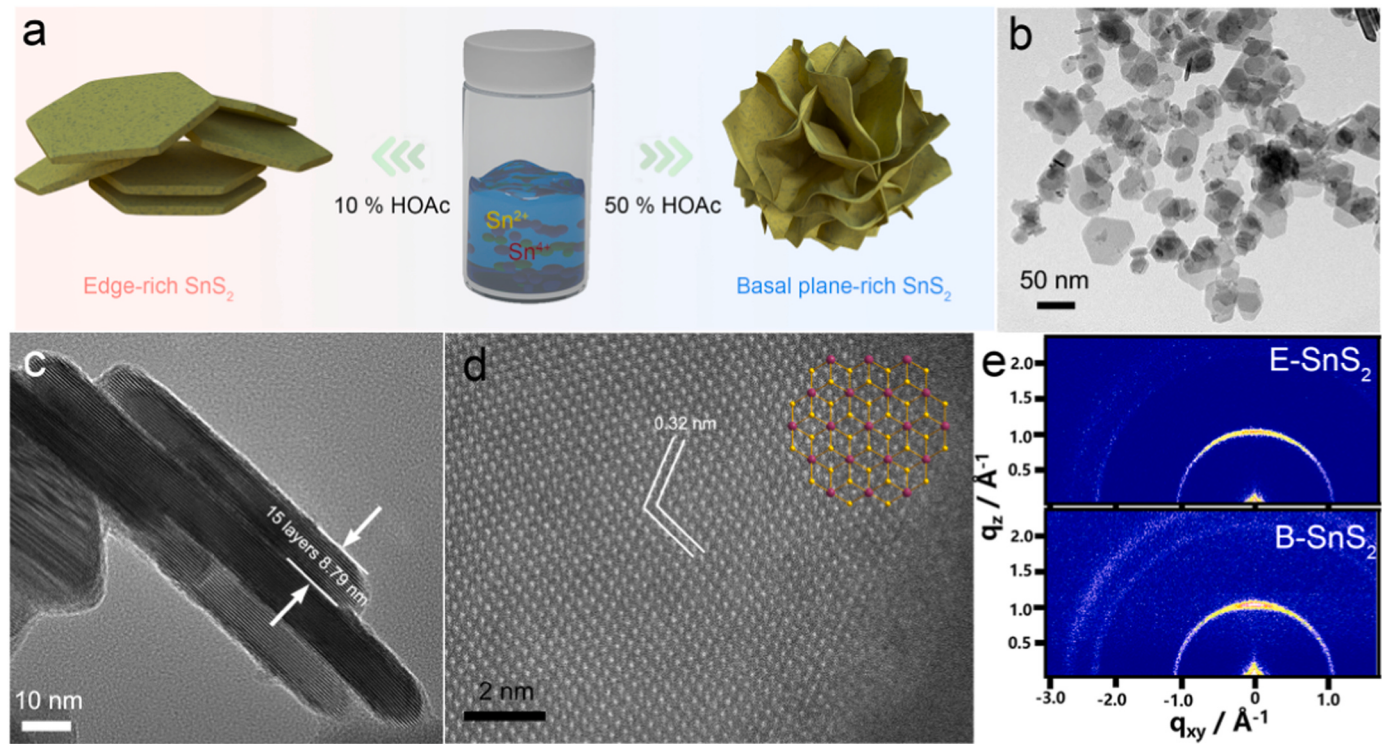
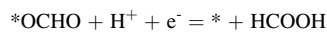
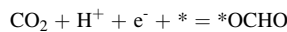
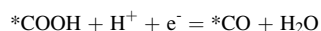
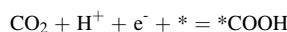


**Fig. 1.** Physical characterization of tin disulfide. (a) Schematic illustration of the synthesis of E-SnS<sub>2</sub> and B-SnS<sub>2</sub>. (b) TEM and (d) aberration-corrected HRTEM images of E-SnS<sub>2</sub>. (e) Comparison of GIWAXS 2D images for E-SnS<sub>2</sub> and B-SnS<sub>2</sub> thin films deposited on a Si substrate.



Carbon Monoxide:



Where \* represents the catalyst slab. The free energy changes of each step were calculated based on the following equations:

$$\Delta G(1) = G(*\text{OCHO}) - G(\text{CO}_2) - G(\text{H}^+ + \text{e}^-) - G(*)$$

$$\Delta G(2) = G(*) + G(\text{HCOOH}) - G(*\text{OCHO}) - G(\text{H}^+ + \text{e}^-)$$

$$\Delta G(3) = G(*\text{COOH}) - G(\text{CO}_2) - G(\text{H}^+ + \text{e}^-) - G(*)$$

$$\Delta G(4) = G(\text{CO}) + G(\text{H}_2\text{O}) - G(*\text{COOH}) - G(\text{H}^+ + \text{e}^-)$$

$$\Delta G(5) = G(*) + G(\text{CO}) - G(*\text{CO})$$

The value of  $G(\text{H}^+ + \text{e}^-)$  is equivalent to 0.5  $G(\text{H}_2)$  based on computational hydrogen electrode (CHE) model. The Gibbs free energy values of non-adsorbed molecules were obtained from previous publications [42,43]. The free energy of \*COOH was corrected by  $-0.25$  eV to account for the contribution of hydrogen bond stabilization effect in aqueous solution [44]. After calculating the total energy of adsorbed intermediates from DFT, the Gibbs free energy was further calculated by VASPKIT software at 298.15 K [45]. The LOBSTER software was used to analyze the chemical bonding in the materials [46–48].

### 3. Results and discussion

#### 3.1. Materials synthesis and characterization

The synthesis of  $\text{SnS}_2$  with Berndtite-2 T phase was conducted through a simple hydrothermal route as illustrated in Fig. 1a. During the process,  $\text{SnCl}_4$  was used as major tin precursor, and  $\text{SnCl}_2$  was added to assist the formation of nanoflakes, of which the proportion of  $\text{SnCl}_2$  is positively correlated with the thickness of the nanoflakes (Fig. S1).  $\text{Sn}^{2+}$  is a soft acid, and  $\text{S}^{2-}$  is a soft base, there's strong bonding strength between them. So it's expected that the presence of  $\text{Sn}^{2+}$  can accelerate the growth of metal chalcogenide. But excess  $\text{SnCl}_2$  leads to the formation of Berndtite-4 H  $\text{SnS}_2$  and small amount of  $\text{SnO}_2$  due to air oxidation (Fig. S2). Therefore,  $\text{SnS}_2$  synthesized with  $\text{Sn}^{2+}/\text{Sn}^{4+} = 0.05/1$  is selected for further analysis and discussion in prospective of concise (denoted as E-SnS<sub>2</sub>). Both XRD and XPS results indicate that E-SnS<sub>2</sub> is only composed of  $\text{SnS}_2$  phase (Fig. S2). The corresponding TEM image (Fig. 1b) reveals that E-SnS<sub>2</sub> is a layered material with lateral size of  $\sim 100$  nm. The nanoflake is constructed by  $\sim 15$  layers of  $\text{SnS}_2$ , stacking with an interlayer distance of 0.58 nm (Fig. 1c). Moreover, lattice fringes indexed to octahedral  $\text{SnS}_2$  with a distance of 0.32 nm was observed on the basal plane (Fig. 1d). Such a nanoflake morphology is favorable to expose edge site in  $\text{SnS}_2$ . Aside of E-SnS<sub>2</sub>, another tin disulfide with larger lateral size was synthesized by adjusting the amount of HOAc used during the synthesis for comparison purpose. The resulting material is also composed of tin disulfide based on XRD measurement (Fig. S3), but the sizes of nanosheets are significantly larger in lateral dimension (Fig. S4). As a result, this control sample predominantly exposes basal sites and is denoted as B-SnS<sub>2</sub>. After coating E-SnS<sub>2</sub> or B-SnS<sub>2</sub> on substrate as thin films, the grazing-incidence wide-angle X-ray scattering (GIWAXS) spectra reveals similar patterns in  $q$ -space, indicating that their orientations are quite similar (Fig. 1e).

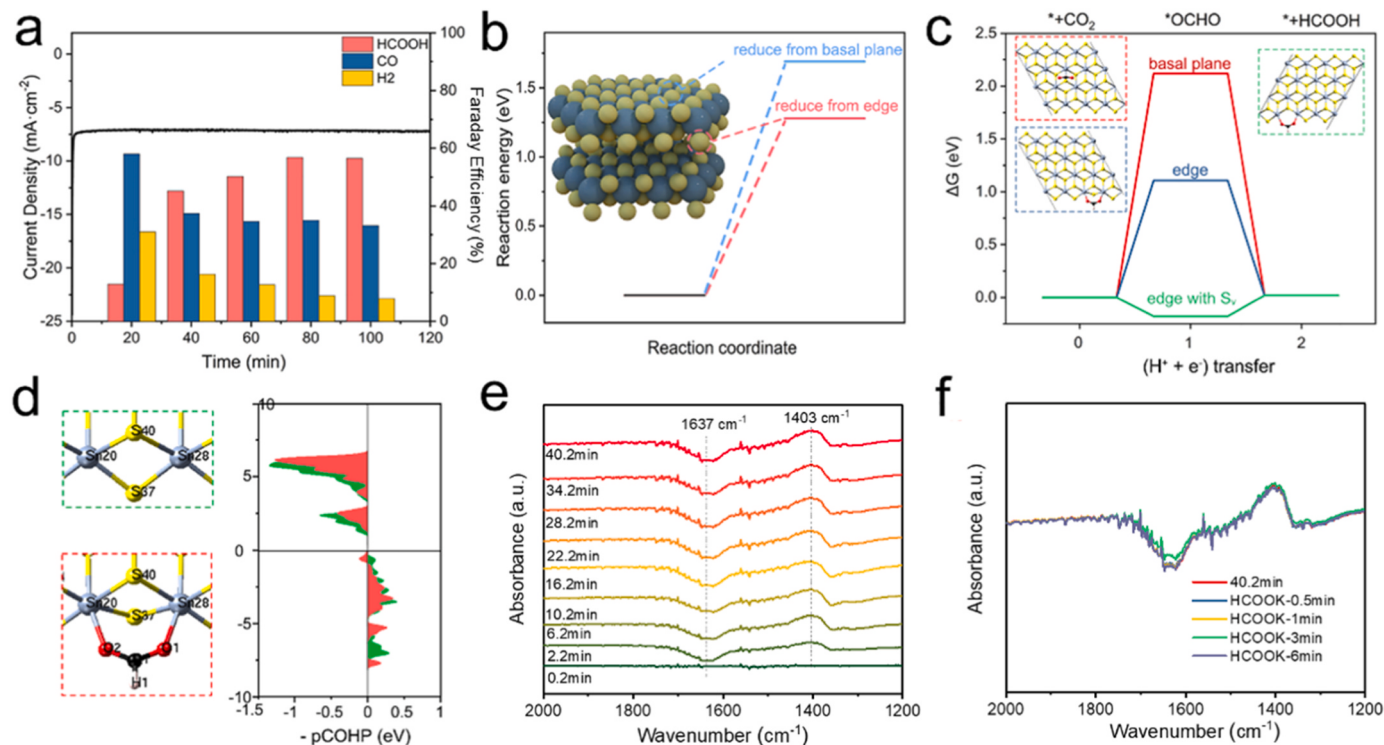


**Fig. 2.** Analysis on the catalyst activation mechanism of E-SnS<sub>2</sub>. (a) i-t curve collected at  $-0.7$  V vs RHE and corresponding FEs for various products along reaction time. (b) Comparison of energy barriers for sulfur vacancy formation at the edge and basal plane of SnS<sub>2</sub>. (c) Free energy change profiles from CO<sub>2</sub> to formate at different sites of SnS<sub>2</sub>. (d) Calculated pCOHP curve of Sn-S bond with (red curve) and without (green curve) \*OCHO intermediate at the edge of SnS<sub>2</sub>. (e) *in-situ* IR spectra of E-SnS<sub>2</sub> under CO<sub>2</sub>RR condition. (f) Comparison of *in-situ* IR spectra before and after addition of 50 mM HCOOK in the electrolyte.

### 3.2. Edge sulfur vacancy induced performance enhancement

The catalytic performance of E-SnS<sub>2</sub> was tested in CO<sub>2</sub>-saturated 0.5 M KHCO<sub>3</sub> solution within an H-cell configuration. It should be noted that the activation of CO<sub>2</sub> is generally achieved under a relatively high cathodic potential, while SnS<sub>2</sub> species tend to undergo a chemical evolution in this potential window [49]. In our case, E-SnS<sub>2</sub> shows cathodic peaks at approximately  $-0.3$  V and  $-0.65$  V vs RHE in the first branch of CV curves, indicating a reduction process (Fig. S5). Therefore, the working electrode coated with E-SnS<sub>2</sub> film was held at a constant potential of  $-0.7$  V to inspect the corresponding structural evolution. The initial reduction process of E-SnS<sub>2</sub> is accompanied by a substantial variation in catalytic selectivity (Fig. 2a). Carbon monoxide (CO) is the dominate product at the initial stage of potentiostatic electrolysis, but its faradaic efficiency decreases significantly as the reaction proceeds. Meanwhile, the hydrogen evolution is obviously suppressed along the reaction and the FE for formate increases from 15% to 60%. On the other hand, the B-SnS<sub>2</sub> doesn't show obvious change of selectivity at the beginning of CO<sub>2</sub> electrolysis, and hydrogen maintains the predominant product through the electrolysis process. These results manifest a catalytic activation process of E-SnS<sub>2</sub>, which is accompanied by the change of catalyst structure under cathodic potential.

To inspect the underlying mechanism of structural evolutions, the catalyst film was characterized after 1 h and 2 h of electrolysis at  $-0.7$  V. The XRD patterns reveal no significant change in phase component after reduction (Fig. S6), and nanoflake morphologies are well retained for both E-SnS<sub>2</sub> and B-SnS<sub>2</sub> (Fig. S7). However, the XPS peaks of Sn 3d shift to lower binding energy after the reduction process (Fig. S8), suggesting the surface of catalyst is reduced. Moreover, in case of E-SnS<sub>2</sub>, some S is detected in the electrolyte after reduction according to the ICP-MS analysis, while Sn is negligible in the electrolyte. On the basis of aforementioned analysis, the reduction process probably induces a dissolution of S element from E-SnS<sub>2</sub> lattices, thereby generating

sulfur vacancies in the material. In contrast, the amount of detached sulfur is relatively small from B-SnS<sub>2</sub>. Based on the physical characterizations of E-SnS<sub>2</sub> and B-SnS<sub>2</sub>, we propose that the distinct performance is correlated with the amount of exposed edge sites. Compared with B-SnS<sub>2</sub>, E-SnS<sub>2</sub> exposes more edges with coordination unsaturated atoms, wherein sulfur vacancy is more likely to generate and favorable for the CO<sub>2</sub>RR.

To investigate the sulfur vacancy formation mechanism and the origin of CO<sub>2</sub> to formate selectivity on SnS<sub>2</sub>, DFT calculation was performed. Upon the formation of sulfur vacancy from stoichiometric SnS<sub>2</sub>, the calculated energy barrier is 0.41 eV lower when the vacancy is located at the edge compared with the basal site (Fig. 2b). This means the sulfur atoms at the edge site of SnS<sub>2</sub> can be removed more easily in thermodynamics. Next the free energy profile from CO<sub>2</sub> to formate conversion was calculated at the basal and edge sites of stoichiometric SnS<sub>2</sub>. The formation of \*OCHO is the potential limiting step, and the energy barriers for basal and edge sites are 2.12, 1.11 eV, respectively, indicating that the latter one is more active for this reaction (Fig. 2c). The geometric analysis of stoichiometric SnS<sub>2</sub> before and after \*OCHO formation indicate that the \*OCHO can influence the bonding environment of edge sulfur (S37). The bond length of S37-Sn20 enlarges from 2.46 to 2.55 Å, indicating the destabilization of this bond upon the adsorption of \*OCHO (Fig. 2d). The bonding strength between S37 and Sn20 is further analyzed by calculating the COHP profile [48], it's clear that some electrons fill in the antibonding orbital after the adsorption of \*OCHO (Fig. 2d). And the ICOHP value changes from  $-2.22$  eV to  $-1.78$  eV. On the basis of aforementioned analysis, the formation of \*OCHO further destabilizes the edge sulfur, which could trigger the reductive elimination of edge sulfur at the beginning of CO<sub>2</sub> electrolysis. We then evaluated the CO<sub>2</sub>RR selectivity at the edge of SnS<sub>2</sub> with sulfur vacancy by DFT calculations. For CO<sub>2</sub> to formate conversion, the formation of \*OCHO is energetically favorable at 0 V vs RHE, and the subsequent step is slightly up hilled by 0.20 eV (Fig. 2c). On the other

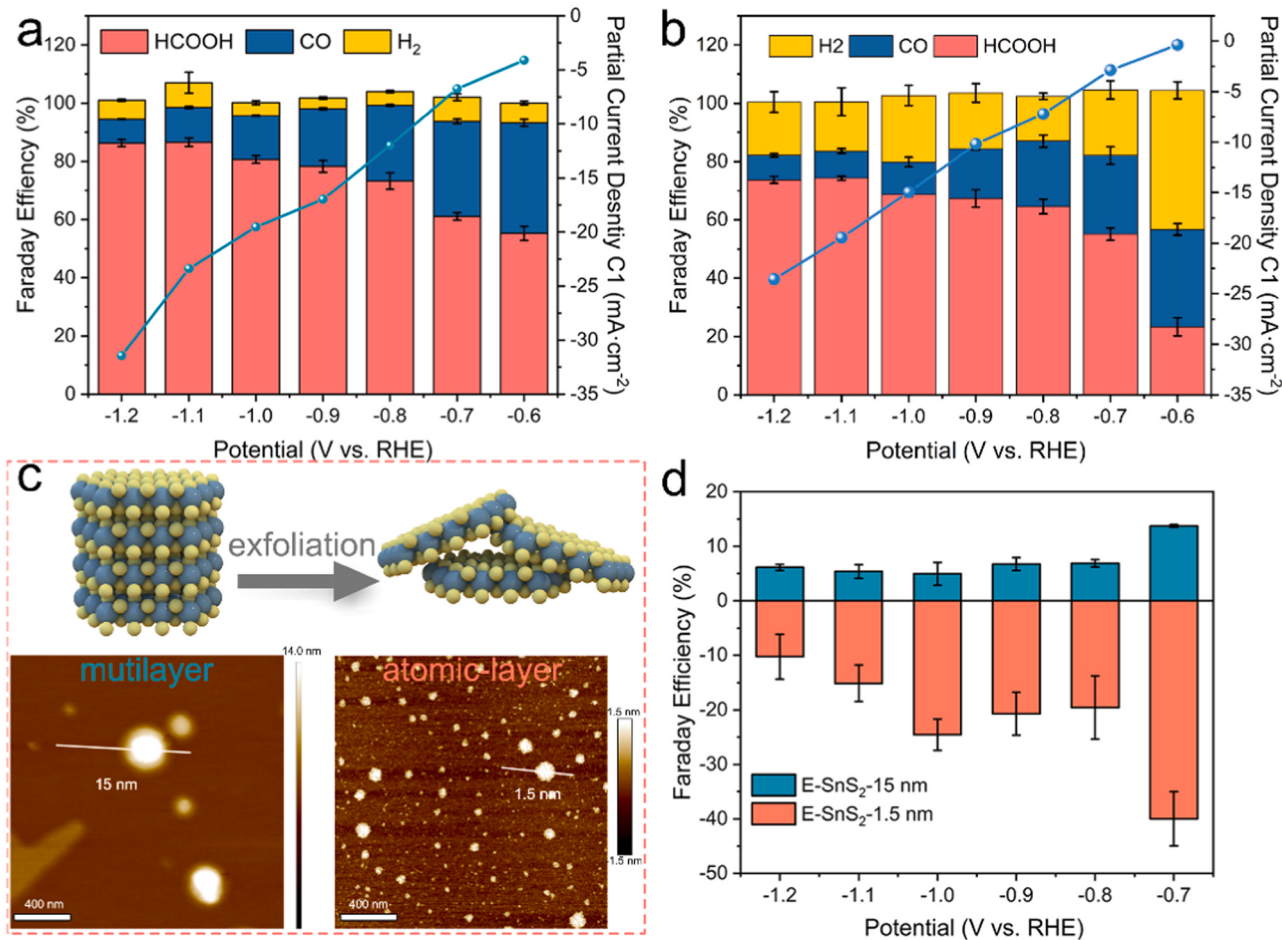


**Fig. 3.** Catalytic performance of samples tested in H type cell in 0.5 M KHCO<sub>3</sub>. FEs for (a) E-SnS<sub>2</sub> and (b) B-SnS<sub>2</sub>. (c) AFM images of E-SnS<sub>2</sub> after exfoliation and (d) corresponding FEs to the HER in E-SnS<sub>2</sub> with different thickness.

hand, for CO<sub>2</sub> to CO conversion, the formation of \*COOH is more difficult compared with \*OCHO as evidenced by the increased free energy for \*COOH formation, suggesting that CO<sub>2</sub> is more likely to be reduced to formate via \*OCHO intermediate at the edge of SnS<sub>2</sub> with sulfur vacancy (Fig. S9). The formation of \*OCHO during the CO<sub>2</sub>RR is confirmed by *in-situ* FTIR (Fig. 2e). The *in-situ* FTIR spectra reveals the absorption band at 1403 cm<sup>-1</sup>, corresponding to \*OCHO key intermediate, and the signal intensity gradually increases with the reaction time, indicating the accumulation of \*OCHO on reduced E-SnS<sub>2</sub> [50,51]. The addition of HCOOK in the electrolyte doesn't change the IR spectra, indicating that the band at 1403 cm<sup>-1</sup> is due to the surface adsorbed \*OCHO intermediate, instead of the HCOO<sup>-</sup> in the solution (Fig. 2f). On the contrary, the downward peak at ca. 1637 cm<sup>-1</sup>, corresponding to water vibration, is observed [52,53]. It's likely due to the replacement of some water molecules around the catalysts' surface by CO<sub>2</sub> reduction intermediates. These results manifest a catalytic activation process of E-SnS<sub>2</sub> triggered by self-reduction of the catalyst, and the resulting sulfur vacancy at the edge sites could contribute to selective CO<sub>2</sub> to formate conversion.

### 3.3. Comparison of CO<sub>2</sub>RR selectivity at edge and basal sites of SnS<sub>2</sub>

After the activation process, the catalytic performance of E-SnS<sub>2</sub> and B-SnS<sub>2</sub> was compared at a broad range of potentials (Fig. 3ab). E-SnS<sub>2</sub> delivers remarkable catalytic performance towards the CO<sub>2</sub>RR with both high selectivity and activity. The FEs for C1 products (HCOO<sup>-</sup> and CO) exceed 90% within the potential range of -0.6 to -1.2 V vs RHE, while the FE for H<sub>2</sub> is below 8%. Such performance is significantly

superior to B-SnS<sub>2</sub>. Based on these experimental measurements, along with the aforementioned DFT calculation results, we conclude that the presence of abundant edges on SnS<sub>2</sub> is important for high selectivity of formate, and the formation of sulfur vacancy at the edges can render the catalysts with even higher performance.

We also noted that the overall morphologies of E-SnS<sub>2</sub> and B-SnS<sub>2</sub> are different. To further inspect the differences of edge and basal sites, E-SnS<sub>2</sub> was exfoliated and nanoflakes with different thickness were collected via differential centrifugation (See materials and methods section for more details). After the exfoliation process, the total number of edge sites remains unchanged, while the amount of basal areas significantly increases. By controlling the centrifugation speed, two catalysts are obtained with different thickness, namely, 15 nm and 1.5 nm (denoted as E-SnS<sub>2</sub>-15 and E-SnS<sub>2</sub>-1.5 nm, respectively), as confirmed by AFM measurement (Fig. 3c). The sample with similar thickness to that of initial E-SnS<sub>2</sub> reveals comparable selectivity towards C1 products. The sample with thinner structure exhibits higher selectivity towards the HER (Fig. 3d, Fig. S10). Considering that thinner nanoflakes expose more basal areas, it's concluded that basal areas of SnS<sub>2</sub> is relatively inert for CO<sub>2</sub> reduction and the basal sites are relatively more active for HER. This conclusion is further supported by the DFT calculations (Fig. S11). The ΔG to generate \*H is ~1.04 eV, much lower than that of \*OCHO (2.12 eV), suggesting that basal plane prefers HER process.

### 3.4. CO<sub>2</sub>RR in flow cell and stability

The Gas diffusion electrode (GDE) decorated with E-SnS<sub>2</sub> was then

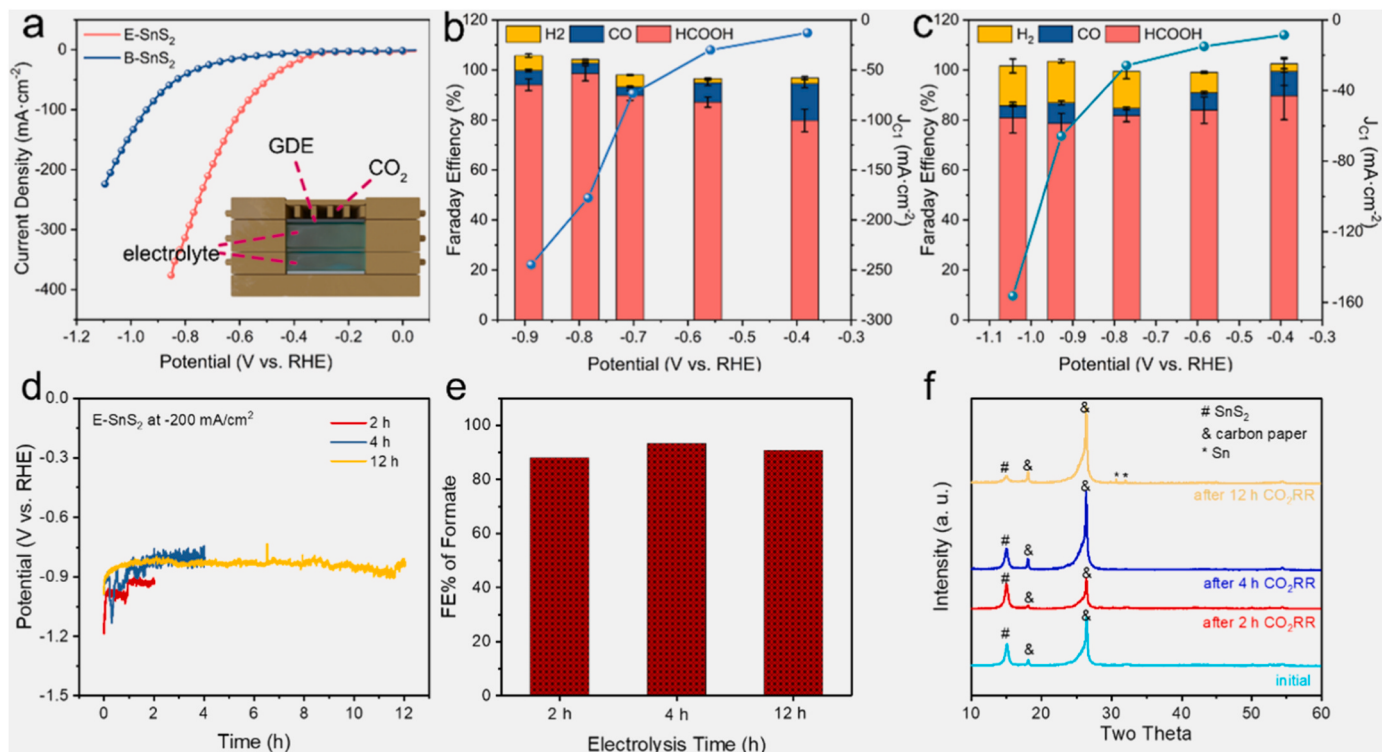


**Fig. 4.** Catalytic performance in flow cell in 1.0 M KOH. (a) LSV curves, FEs for various products by using (b) E-SnS<sub>2</sub> and (c) B-SnS<sub>2</sub> as catalyst, (d) Stability test of E-SnS<sub>2</sub> under a current density of  $-200 \text{ mA}\cdot\text{cm}^{-2}$  and (e) FE% of formate after different times of electrolysis. (f) XRD patterns of E-SnS<sub>2</sub> after different times of electrolysis.

assembled in a flow cell, wherein the sufficient supply of CO<sub>2</sub> enables electrolyzer to operate at the current densities required for industrial deployment. The flow cell setup is illustrated in Fig. S12. Accordingly, E-SnS<sub>2</sub> reaches a current density of  $-100 \text{ mA}\cdot\text{cm}^{-2}$  at a small potential of  $-0.6 \text{ V}$  vs RHE and approaches to a large current density of  $-400 \text{ mA}\cdot\text{cm}^{-2}$  within  $-0.9 \text{ V}$  vs RHE (Fig. 4a). In addition, the hydrogen evolution is efficiently suppressed in alkaline solution, resulting in higher CO<sub>2</sub>RR selectivity. The FEs of C1 products are over 95% in wide potential values ranging from  $-0.4$  to  $-0.9 \text{ V}$  vs RHE and formate is the predominant product (Fig. 4b). Such high activity and selectivity induce a desirable energy efficiency (Fig. S13). In contrast, B-SnS<sub>2</sub> deliveries an inferior catalytic selectivity (Fig. 4c). Furthermore, E-SnS<sub>2</sub> exhibits robust stability in flow cell (Fig. 4d). A steady curve was obtained at industrial desirable current density of  $-200 \text{ mA}\cdot\text{cm}^{-2}$  and persisted for at least 12 h. The FEs towards formate was retained at approximately 90% after 2 h, 4 h and 12 h's electrolysis (Fig. 4e).

During the long term bulk electrolysis, we found that the amount of catalyst on GDE was decreasing over time, as confirmed by the weakening of diffraction signal at  $\sim 15^\circ$  in the XRD patterns, indicating the peeling of catalyst during long term CO<sub>2</sub>RR (Fig. 4f). To understand why the formate selectivity was not changed when the catalyst amount on GDE decreased, various amounts of E-SnS<sub>2</sub> was air brushed on GDE to study the influence of catalyst loading. As shown in Fig. S14, when the catalyst loading is within  $0.8 \sim 4 \text{ mg}/\text{cm}^2$ , the selectivity towards formate maintains in the range of 75% to  $\sim 90\%$ , only when the catalyst loading is very low, the FE% of formate plunges significantly. This is because in GDE, the CO<sub>2</sub> is reduced at the triple interface composed of electrolyte, catalyst and gas, as long as the catalyst can cover the entire GDE, further increasing the loading would not promote the selectivity. At 2 h and 4 h time point, no additional peaks in XRD were found other than diffraction patterns of SnS<sub>2</sub> and carbon paper substrate. However, after 12 h's electrolysis, two minor peaks at  $30.65^\circ$  and  $32.04^\circ$  show up, which is due to the formation of metallic tin. Aside of catalyst peeling from GDE, salt deposition and flooding issue were observed during flow

cell measurement, which make even longer electrolysis difficult.

#### 4. Conclusion

In summary, we synthesized layered SnS<sub>2</sub> with different lateral sizes. The small one (E-SnS<sub>2</sub>) exhibits higher selectivity and activity towards formate in CO<sub>2</sub>RR. Based on experimental characterization and DFT results, the edge site of SnS<sub>2</sub> with sulfur vacancy is much more active for CO<sub>2</sub> to formate conversion compared with basal sites. Due to the presence of active edge sites, a high current density of  $-200 \text{ mA}\cdot\text{cm}^{-2}$  and a FE of  $\sim 90\%$  for formate is achieved at  $\sim -0.84 \text{ V}$  vs RHE in 1.0 M KOH in a flow cell, and it is stable for at least 12 h. This work is important for the design of layered materials for CO<sub>2</sub>RR.

#### CRediT authorship contribution statement

**Zhipeng Liu:** Methodology, Investigation, Validation, Data curation, Writing – original draft. **Chang Liu:** Investigation. **Jiawei Zhang:** Writing – review & editing. **Suhua Mao:** Investigation. **Xiao Liang:** Methodology. **Hanlin Hu:** Methodology. **Xiaoxi Huang:** Conceptualization, Investigation, Validation, Data curation, Writing – original draft, Writing – review & editing.

#### Declaration of Competing Interest

The authors declare that they have no known competing financial interests or personal relationships that could have appeared to influence the work reported in this paper.

#### Data Availability

Data will be made available on request.

## Acknowledgments

This study was supported by the Guangdong Natural Science Foundation (2022A1515110034, 2023A1515011408) and Innovation Team Project of Guangdong (2022KCXTD055), and the Shenzhen Government's Plan of Science and Technology (GXWD20201231165806004, JCYJ20220811141844002). We also acknowledge Xin Li on helping the catalyst synthesis and CO<sub>2</sub>RR performance evaluation.

## Appendix A. Supporting information

Supplementary data associated with this article can be found in the online version at [doi:10.1016/j.apcatb.2023.123274](https://doi.org/10.1016/j.apcatb.2023.123274).

## References

- [1] P. De Luna, C. Hahn, D. Higgins, S.A. Jaffer, T.F. Jaramillo, E.H. Sargent, What would it take for renewably powered electrosynthesis to displace petrochemical processes? *Science* 364 (2019) eaav3506, <https://doi.org/10.1126/science.aav3506>.
- [2] W. Ma, X. He, W. Wang, S. Xie, Q. Zhang, Y. Wang, Electrocatalytic reduction of CO<sub>2</sub> and CO to multi-carbon compounds over Cu-based catalysts, *Chem. Soc. Rev.* 50 (2021) 12897–12914, <https://doi.org/10.1039/D1CS00535A>.
- [3] Y. Cheng, P. Hou, X. Wang, P. Kang, CO<sub>2</sub> electrolysis system under industrially relevant conditions, *Acc. Chem. Res.* 55 (2022) 231–240, <https://doi.org/10.1021/acs.accounts.1c00614>.
- [4] M. Yu, P.F. Sui, X.Z. Fu, J.L. Luo, S. Liu, Specific metal nanostructures toward electrochemical CO<sub>2</sub> reduction: recent advances and perspectives, *Adv. Energy Mater.* 13 (2022), 2203191, <https://doi.org/10.1002/aenm.202203191>.
- [5] S. Nitopi, E. Bertheussen, S.B. Scott, X. Liu, A.K. Engstfeld, S. Horch, B. Seger, I.E. L. Stephens, K. Chan, C. Hahn, J.K. Nørskov, T.F. Jaramillo, I. Chorkendorff, Progress and perspectives of electrochemical CO<sub>2</sub> reduction on copper in aqueous electrolyte, *Chem. Rev.* 119 (2019) 7610–7672, <https://doi.org/10.1021/acs.chemrev.8b00705>.
- [6] X. Duan, J. Xu, Z. Wei, J. Ma, S. Guo, S. Wang, H. Liu, S. Dou, Metal-free carbon materials for CO<sub>2</sub> electrochemical reduction, *Adv. Mater.* 29 (2017), <https://doi.org/10.1002/adma.201701784>.
- [7] P. Saha, S. Amanullah, A. Dey, Selectivity in electrochemical CO<sub>2</sub> reduction, *Acc. Chem. Res.* 55 (2022) 134–144, <https://doi.org/10.1021/acs.accounts.1c00678>.
- [8] S. Zhao, Y. Yang, Z. Tang, Insight into structural evolution, active sites, and stability of heterogeneous electrocatalysts, *Angew. Chem. Int. Ed.* 61 (2022), e202110186, <https://doi.org/10.1002/anie.202110186>.
- [9] K.S. Novoselov, A.K. Geim, S.V. Morozov, D. Jiang, Y. Zhang, S.V. Dubonos, I. V. Grigorieva, A.A. Firsov, Electric field effect in atomically thin carbon films, *Science* 306 (2004) 666–669, <https://doi.org/10.1126/science.1102896>.
- [10] C. Tan, X. Cao, X.J. Wu, Q. He, J. Yang, X. Zhang, J. Chen, W. Zhao, S. Han, G. H. Nam, M. Sindoro, H. Zhang, Recent advances in ultrathin two-dimensional nanomaterials, *Chem. Rev.* 117 (2017) 6225–6331, <https://doi.org/10.1039/d0nr05746k>.
- [11] X. Chia, M. Pumera, Layered transition metal dichalcogenide electrochemistry: journey across the periodic table, *Chem. Soc. Rev.* 47 (2018) 5602–5613, <https://doi.org/10.1039/c7cs00846e>.
- [12] D. Voiry, H. Yamaguchi, J. Li, R. Silva, D.C. Alves, T. Fujita, M. Chen, T. Asefa, V. Shenoy, G. Eda, M. Chhowalla, Enhanced catalytic activity in strained chemically exfoliated WS<sub>2</sub> nanosheets for hydrogen evolution, *Nat. Mater.* 12 (2013) 850–855, <https://doi.org/10.1038/nmat3700>.
- [13] D. Voiry, J. Yang, M. Chhowalla, Recent strategies for improving the catalytic activity of 2D TMD nanosheets toward the hydrogen evolution reaction, *Adv. Mater.* 28 (2016) 6197–6206, <https://doi.org/10.1002/adma.201505597>.
- [14] K.K. Mohammad Asadi, Cong Liu, Aditya Venkata Addepalli, Pedram Abbasi, Poya Yasaee, Patrick Phillips, Amirhossein Behranginia, José M. Cerrato, Richard Haasch, Peter Zapal, Bijendra Kumar, Robert F. Klie, Jeremiah Abiade, Larry A. Curtiss, Amin Salehi-Khojin, Nanostructured transition metal dichalcogenide electrocatalysts for CO<sub>2</sub> reduction in ionic liquid, *Science* 353 (2016) 467–470, <https://doi.org/10.1126/science.aaf4767>.
- [15] D. Merki, X. Hu, Recent developments of molybdenum and tungsten sulfides as hydrogen evolution catalysts, *Energy Environ. Sci.* 4 (2011) 3878, <https://doi.org/10.1039/C1EE01970H>.
- [16] J.N. Coleman, M. Lotya, A. O'Neill, S.D. Bergin, P.J. King, U. Khan, K. Young, A. Gaucher, S. De, R.J. Smith, I.V. Shvets, S.K. Arora, G. Stanton, H.Y. Kim, K. Lee, G.T. Kim, G.S. Duesberg, T. Hallam, J.J. Boland, J.J. Wang, J.F. Donegan, J. C. Grunlan, G. Moriarty, A. Shmeliov, R.J. Nicholls, J.M. Perkins, E.M. Grieveson, K. Theuwissen, D.W. McComb, P.D. Nellist, V. Nicolosi, Two-dimensional nanosheets produced by liquid exfoliation of layered materials, *Science* 331 (2011) 568–571, <https://doi.org/10.1126/science.1194975>.
- [17] J.S. Kim, J. Kim, J. Zhao, S. Kim, J.H. Lee, Y. Jin, H. Choi, B.H. Moon, J.J. Bae, Y. H. Lee, S.C. Lim, Electrical transport properties of polymeric MoS<sub>2</sub>, *ACS Nano* 10 (2016) 7500–7506, <https://doi.org/10.1021/acsnano.6b02267>.
- [18] R. Lv, J.A. Robinson, R.E. Schaak, D. Sun, Y. Sun, T.E. Mallouk, M. Terrones, Transition metal dichalcogenides and beyond: synthesis, properties, and applications of single- and few-layer nanosheets, *Acc. Chem. Res.* 48 (2015) 56–64, <https://doi.org/10.1021/ar5002846>.
- [19] R. Yang, Y. Fan, L. Mei, H.S. Shin, D. Voiry, Q. Lu, J. Li, Z. Zeng, Synthesis of atomically thin sheets by the intercalation-based exfoliation of layered materials, *Nat. Synth.* 2 (2023) 101–118, <https://doi.org/10.1038/s44160-022-00232-z>.
- [20] A.M. van der Zande, P.Y. Huang, D.A. Chenet, T.C. Berkelbach, Y. You, G.H. Lee, T. F. Heinz, D.R. Reichman, D.A. Muller, J.C. Hone, Grains and grain boundaries in highly crystalline monolayer molybdenum disulfide, *Nat. Mater.* 12 (2013) 554–561, <https://doi.org/10.1038/nmat3633>.
- [21] D.H. Keum, S. Cho, J.H. Kim, D.-H. Choe, H.-J. Sung, M. Kan, H. Kang, J.-Y. Hwang, S.W. Kim, H. Yang, K.J. Chang, Y.H. Lee, Bandgap opening in few-layered monoclinic MoTe<sub>2</sub>, *Nat. Phys.* 11 (2015) 482–486, <https://doi.org/10.1038/nphys3314>.
- [22] Q.H. Wang, K. Kalantar-Zadeh, A. Kis, J.N. Coleman, M.S. Strano, Electronics and optoelectronics of two-dimensional transition metal dichalcogenides, *Nat. Nanotechnol.* 7 (2012) 699–712, <https://doi.org/10.1038/nano.2012.193>.
- [23] T.F. Jaramillo, K.P. Jorgensen, J. Bonde, J.H. Nielsen, S. Horch, I. Chorkendorff, Identification of active edge sites for electrochemical H<sub>2</sub> evolution from MoS<sub>2</sub> nanocatalysts, *Science* 317 (2007) 100–102, <https://doi.org/10.1126/science.1141483>.
- [24] P.G.M. Berit Hinnemann, Jacob Bonde, Kristina P. Jørgensen, Jane H. Nielsen, Sebastian Horch, Ib Chorkendorff, Jens K. Nørskov, Biomimetic hydrogen evolution MoS<sub>2</sub> nanoparticles as catalyst for hydrogen evolution, *J. Am. Chem. Soc.* 127 (2005) 5308–5309, <https://doi.org/10.1021/ja0504690>.
- [25] Y. Li, H. Wang, L. Xie, Y. Liang, G. Hong, H. Dai, MoS<sub>2</sub> nanoparticles grown on graphene: an advanced catalyst for the hydrogen evolution reaction, *J. Am. Chem. Soc.* 133 (2011) 7296–7299, <https://doi.org/10.1021/ja201269b>.
- [26] J. Kibsgaard, Z. Chen, B.N. Reinecke, T.F. Jaramillo, Engineering the surface structure of MoS<sub>2</sub> to preferentially expose active edge sites for electrocatalysis, *Nat. Mater.* 11 (2012) 963–969, <https://doi.org/10.1038/nmat3439>.
- [27] D. Kong, H. Wang, J.J. Cha, M. Pasta, K.J. Koski, J. Yao, Y. Cui, Synthesis of MoS<sub>2</sub> and MoSe<sub>2</sub> films with vertically aligned layers, *Nano Lett.* 13 (2013) 1341–1347, <https://doi.org/10.1021/nl400258t>.
- [28] B. Ni, X. Wang, Face the edges: catalytic active sites of nanomaterials, *Adv. Sci.* 2 (2015), 1500085, <https://doi.org/10.1002/advs.201500085>.
- [29] Y. Shan, Y. Li, H. Pang, Applications of tin sulfide-based materials in lithium-ion batteries and sodium-ion batteries, *Adv. Funct. Mater.* 30 (2020), 2001298, <https://doi.org/10.1002/adfm.202001298>.
- [30] J. He, X. Liu, H. Liu, Z. Zhao, Y. Ding, J. Luo, Highly selective electrocatalytic reduction of CO<sub>2</sub> to formate over Tin(IV) sulfide monolayers, *J. Catal.* 364 (2018) 125–130, <https://doi.org/10.1016/j.jchemosphere.2021.132889>.
- [31] A. Zhang, Y. Liang, H. Li, S. Wang, Q. Chang, K. Peng, Z. Geng, J. Zeng, Electronic tuning of SnS<sub>2</sub> nanosheets by hydrogen incorporation for efficient CO<sub>2</sub> electroreduction, *Nano Lett.* 21 (2021) 7789–7795, <https://doi.org/10.1021/acs.nanolett.1c02757>.
- [32] H. Cheng, S. Liu, J. Zhang, T. Zhou, N. Zhang, X.S. Zheng, W. Chu, Z. Hu, C. Wu, Y. Xie, Surface nitrogen-injection engineering for high formation rate of CO<sub>2</sub> reduction to formate, *Nano Lett.* 20 (2020) 6097–6103, <https://doi.org/10.1021/acs.nanolett.0c02144>.
- [33] Y. Li, W. Niu, T. Chen, Y. Sun, M. Yu, Integrating vacancy engineering and energy-level adapted coupling of electrocatalyst for enhancement of carbon dioxide conversion, *Appl. Catal. B Environ.* 321 (2023), 122037, <https://doi.org/10.1016/j.apcatb.2022.122037>.
- [34] Z. Liu, C. Liu, S. Mao, X. Huang, Heterogeneous structure of Sn/SnO<sub>2</sub> constructed via phase engineering for efficient and stable CO<sub>2</sub> reduction, *ACS Appl. Mater. Interfaces* 15 (2023) 7529–7537, <https://doi.org/10.1021/acsami.2c18522>.
- [35] H.C.Yongfu Sun, Shan Gao, Zhihu Sun, Qinghui Liu, Qin Liu, Fengcai Lei, Tao Yao, Jingfu He, Shiqiang Wei, Yi Xie, Freestanding tin disulfide single-layers realizing efficient visible-light water splitting, *Angew. Chem. Int. Ed.* 51 (2012) 8727–8731, <https://doi.org/10.1002/anie.201204675>.
- [36] J. Zhang, Z. Liu, H. Guo, H. Lin, H. Wang, X. Liang, H. Hu, Q. Xia, X. Zou, X. Huang, Selective, stable production of ethylene using a pulsed Cu-based electrode, *ACS Appl. Mater. Interfaces* 14 (2022) 19388–19396, <https://doi.org/10.1021/acsami.2e01230>.
- [37] G.F. Kresse, Efficient iterative schemes for ab initio total-energy calculations using a plane-wave basis set, *Phys. Rev. B* 54 (1996) 11169–11186, <https://doi.org/10.1103/physrevb.54.11169>.
- [38] G.K.J.F. uller, Efficiency of ab-initio total energy calculations for metals and semiconductors using a plane-wave basis set, *Comput. Mat. Sci.* 6 (1996) 15–50, [https://doi.org/10.1016/0927-0256\(96\)00008-0](https://doi.org/10.1016/0927-0256(96)00008-0).
- [39] G. Kresse, D. Joubert, From ultrasoft pseudopotentials to the projector augmented-wave method, *Phys. Rev. B* 59 (1999) 1758–1775, <https://doi.org/10.1103/PhysRevB.59.1758>.
- [40] J.P. Perdew, K. Burke, M. Ernzerhof, Generalized gradient approximation made simple, *Phys. Rev. Lett.* 77 (1996) 3865–3868, <https://doi.org/10.1103/PhysRevLett.77.3865>.
- [41] S. Grimme, J. Antony, S. Ehrlich, H. Krieg, A consistent and accurate ab initio parametrization of density functional dispersion correction (DFT-D) for the 94 elements H–Pu, *J. Chem. Phys.* 132 (2010), 154104, <https://doi.org/10.1063/1.3382344>.
- [42] A. Klinkova, P. De Luna, C.-T. Dinh, O. Voznyy, E.M. Larin, E. Kumacheva, E. H. Sargent, Rational design of efficient palladium catalysts for electroreduction of carbon dioxide to formate, *ACS Catal.* 6 (2016) 8115–8120, <https://doi.org/10.1021/acscatal.6b01719>.
- [43] Z. Liu, J. Chen, H. Guo, X. Huang, Reduction-tolerant SnO<sub>2</sub> assisted by surface hydroxyls for selective CO<sub>2</sub> electroreduction to formate over wide potential range,

- Nano Energy 108 (2023), 108193, <https://doi.org/10.1016/j.nanoen.2023.108193>.
- [44] X. Zheng, P. De Luna, F.P. García de Arquer, B. Zhang, N. Becknell, M.B. Ross, Y. Li, M.N. Banis, Y. Li, M. Liu, O. Voznyy, C.T. Dinh, T. Zhuang, P. Stadler, Y. Cui, X. Du, P. Yang, E.H. Sargent, Sulfur-modulated tin sites enable highly selective electrochemical reduction of CO<sub>2</sub> to formate, Joule 1 (2017) 794–805, <https://doi.org/10.1016/j.joule.2017.09.014>.
- [45] V. Wang, N. Xu, J.-C. Liu, G. Tang, W.-T. Geng, VASPKIT: a user-friendly interface facilitating high-throughput computing and analysis using VASP code, Comput. Phys. Commun. 267 (2021), 108033, <https://doi.org/10.1016/j.cpc.2021.108033>.
- [46] R. Nelson, C. Ertural, J. George, V.L. Deringer, G. Hautier, R. Dronskowski, LOBSTER: local orbital projections, atomic charges, and chemical-bonding analysis from projector-augmented-wave-based density-functional theory, J. Comput. Chem. 41 (2020) 1931–1940, <https://doi.org/10.1002/jcc.26353>.
- [47] S. Maintz, V.L. Deringer, A.L. Tchougreeff, R. Dronskowski, LOBSTER: a tool to extract chemical bonding from plane-wave based DFT, J. Comput. Chem. 37 (2016) 1030–1035, <https://doi.org/10.1002/jcc.24300>.
- [48] V.L. Deringer, A.L. Tchougreeff, R. Dronskowski, Crystal orbital Hamilton population (COHP) analysis as projected from plane-wave basis sets, J. Phys. Chem. A 115 (2011) 5461–5466, <https://doi.org/10.1021/jp202489s>.
- [49] F. Li, L. Chen, M. Xue, T. Williams, Y. Zhang, D.R. MacFarlane, J. Zhang, Towards a better Sn: efficient electrocatalytic reduction of CO<sub>2</sub> to formate by Sn/SnS<sub>2</sub> derived from SnS<sub>2</sub> nanosheets, Nano Energy 31 (2017) 270–277, <https://doi.org/10.1016/j.nanoen.2016.11.004>.
- [50] Y. Cheng, J. Hou, P. Kang, Integrated capture and electroreduction of flue gas CO<sub>2</sub> to formate using amine functionalized SnO<sub>x</sub> nanoparticles, ACS Energy Lett. 6 (2021) 3352–3358, <https://doi.org/10.1021/acsenergylett.1c01553>.
- [51] Z. Wu, H. Wu, W. Cai, Z. Wen, B. Jia, L. Wang, W. Jin, T. Ma, Engineering Bismuth-Tin interface in bimetallic aerogel with a 3D porous structure for highly selective electrocatalytic CO<sub>2</sub> reduction to HCOOH, Angew. Chem. Int. Ed. 60 (2021) 12554–12559, <https://doi.org/10.1002/anie.202102832>.
- [52] M.F. Baruch, J.E. Pander III, J.L. White, A.B. Bocarsly, Mechanistic insights into the reduction of CO<sub>2</sub> on tin electrodes using in situ ATR-IR spectroscopy, ACS Catal. 5 (2015) 3148–3156, <https://doi.org/10.1021/acscatal.5b00402>.
- [53] T. Wang, J. Chen, X. Ren, J. Zhang, J. Ding, Y. Liu, K.H. Lim, J. Wang, X. Li, H. Yang, Y. Huang, S. Kawi, B. Liu, Halogen-incorporated Sn catalysts for selective electrochemical CO<sub>2</sub> reduction to formate, Angew. Chem. Int. Ed. 62 (2023), e202211174, <https://doi.org/10.1002/anie.202211174>.